PHILOSOPHICAL TRANSACTIONS A

royalsocietypublishing.org/journal/rsta

Research

Cite this article: Nieves MJ, Brun M. 2019 Dynamic characterization of a periodic microstructured flexural system with rotational inertia. *Phil. Trans. R. Soc. A* **377**: 20190113.
http://dx.doi.org/10.1098/rsta.2019.0113

Accepted: 26 June 2019

One contribution of 14 to a theme issue 'Modelling of dynamic phenomena and localization in structured media (part 1)'.

Subject Areas:
applied mathematics, mathematical modelling, mechanics, wave motion

Keywords:
microstructured medium, dispersion relation, flexural waves, Rayleigh beams

Author for correspondence:
Michael Nieves
e-mail: m.nieves@keele.ac.uk

Electronic supplementary material is available online at https://doi.org/10.6084/m9.figshare.c.4588604.

THE ROYAL SOCIETY PUBLISHING

Dynamic characterization of a periodic microstructured flexural system with rotational inertia

M. J. Nieves[1,2] and M. Brun[2]

[1]School of Computing and Mathematics, Keele University, Keele ST5 5BG, UK
[2]Department of Mechanical, Chemical and Material Engineering, University of Cagliari, Cagliari 09123, Italy

MJN, 0000-0003-4616-4548

We consider the propagation of waves in a flexural medium composed of massless beams joining a periodic array of elements, elastically supported and possessing mass and rotational inertia. The dispersion properties of the system are determined and the influence and interplay between the dynamic parameters on the structure of the pass and stop bands are analysed in detail. We highlight the existence of three special dynamic regimes corresponding to a low stiffness in the supports and/or low rotational inertia of the masses; to a high stiffness and/or high rotational inertia regime; and to a transition one where dispersion degeneracies are encountered. In the low-frequency regime, a rigorous asymptotic analysis shows that the structure approximates a continuous Rayleigh beam on an elastic foundation.

This article is part of the theme issue 'Modelling of dynamic phenomena and localization in structured media (part 1)'.

1. Introduction

Microstructure is a powerful concept that is currently driving the design of mechanical metamaterials capable of controlling vibrations and enabling various dynamic effects, having analogues in electromagnetism and optics, for a wide variety of applications. Many of these effects have been shown to be achievable in periodic systems formed from arrays of masses connected by elastic

rods. Here, we consider an elastically supported one-dimensional discrete flexural system, where the contribution of the rotational inertia at the nodal points is taken into account. In particular, we show that the support stiffness and rotational inertia can combine to create special dynamic phenomena. Euler–Bernoulli (EB) structures have been analysed in great detail in [1], including effects of pre-stress and damage in [2,3].

Recently, there has been an effort to design microstructured flexural materials that use Rayleigh beams, i.e. beam elements with rotational inertia [4]. In flexural systems, this physical property is significant in obtaining effects including negative refraction, dynamic anisotropy and neutrality brought by dispersive degeneracies, as shown in [5] for two-dimensional networks of Rayleigh beams. Methods for creating focusing and localization by using Rayleigh beam-made waveguides in square-cell lattices have been demonstrated in [6], while transmission problems for a hexagonal Rayleigh beam-lattice interface have been studied in [7]. Furthermore, flexural systems allow for the modelling of mechanical phenomena not usually encountered in spring systems adding a greater flexibility in designing methods for achieving special dispersive properties. In this sense, we mention the in-plane lattice problem considered in [8], where the use of prestressed Rayleigh beams and concentrated pulsating moments were used to achieve topological modes and the design of an efficient flat lens, and [9] where a recipe for tuning the mechanical properties of a flexural lattice to obtain dynamic anisotropy and 'isotropization' is described. The Lagrangian approach to modelling the dynamic response of structured flexural chiral materials has been used in [10], where the influence of resonators on the lattice acoustic behaviour was studied and in [11], where vibration of lattices with distributed masses with rotational inertia was also investigated with micro-polar continuum approximations of the lattice. Asymptotic approximations have been employed in [12] to determine the dispersive nature of chiral auxetic beam lattices containing resonators.

Flexural structures have a great range of applicability. In addition to representing the microstructure of flexural medium, they also possess applications in the design of large scale structures found in structural engineering such as bridges and buildings [13,14]. Additionally, waves in discrete systems may initiate, support or enhance failure modes [15]. The bending modes of two-dimensional flexural systems with stationary cracks have been considered in [16]. The response of a three-dimensional flexural structure with a static crack subjected to mode III loading is investigated in [17]. A class of mass-beam systems undergoing phase transition in response to gravitational or thermal loads have been recently studied in [18–20]. Analytical and numerical studies of mass-beam systems undergoing collapse sustained by vibrational loads have appeared in [21,22]. The analysis of quasi-static damage propagation in two-dimensional beam lattices has been carried out in [23,24].

Here, we consider a particular one-dimensional discrete flexural system, formed from massless beams connecting periodically placed masses as in figure 1. We show this structure possesses several special dynamic features with various technological applications, arising from the combination of the rotational inertia introduced at the junctions and the properties of the transverse supports. Moreover, the rotational inertia brings high-frequency passbands implying that additional failure modes supported by high-frequency loads may be sustained by this medium.

In §2, the structure and the equations governing its motion are presented. In §3, we consider the low-frequency limit of the medium and we show this system represents a Rayleigh beam supported by a Winkler foundation. Through a parametric analysis, we completely characterize the dispersive nature of the medium and show that the interplay of the support stiffness and rotational inertia can lead to special dynamic features (see §4). Finally, in §5, we give some conclusions.

2. Modelling a supported mass-beam chain

We consider the dynamic problem of the infinite heterogeneous structured medium shown in figure 1, which is composed of nodal masses and flexural elastic connections. The nodal points, at

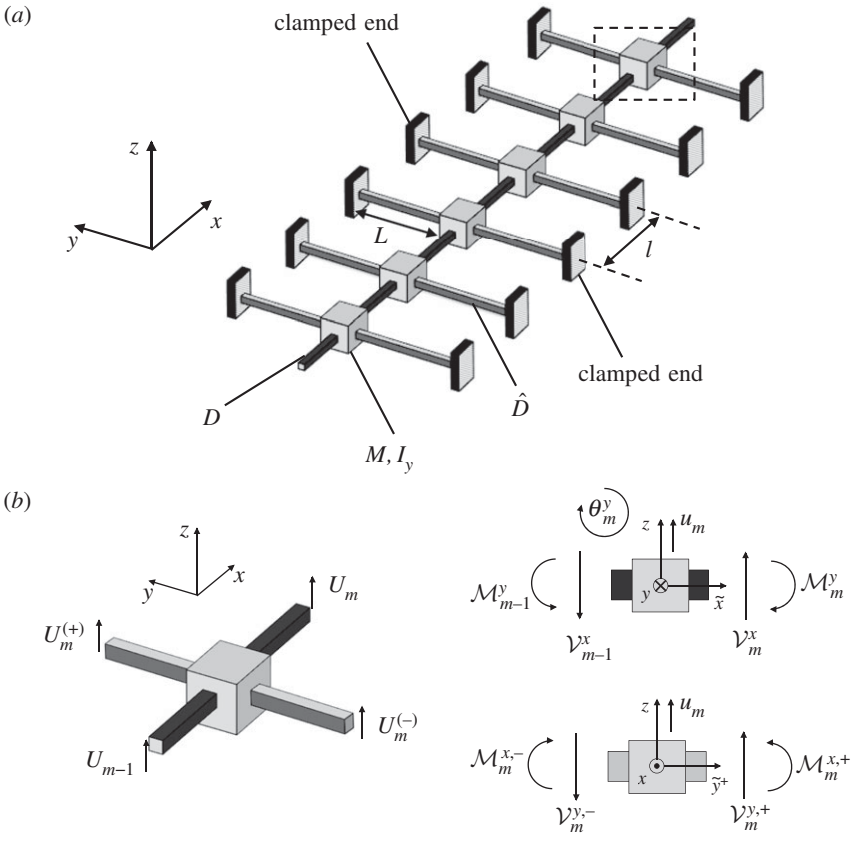

Figure 1. (*a*) The structured medium composed of inertial nodes connected by massless elastic beams along the *x*-direction. Each mass is supported by transverse beams in the *y*-direction. (*b*) On the left panel, we report the notation and the sign convention for the transverse displacements U_{m-1} and U_m in the longitudinal connections and for the transverse displacements $U_m^{(+)}$ and $U_m^{(-)}$ in the lateral ones. On the right panel, we show the sign convention for positive directions of displacements u_m, rotations θ_m^y, bending moments $\mathcal{M}_{m-1}^y$, $\mathcal{M}_m^y$ and $\mathcal{M}_m^{x,\pm}$, and shear forces $\mathcal{V}_{m-1}^x$, $\mathcal{V}_m^x$ and $\mathcal{V}_m^{y,\pm}$. The local coordinates $\tilde{x}$ and $\tilde{y}^\pm$ are defined in the electronic supplementary material.

$x = lm$ ($m = 0, \pm1, \pm2, \ldots$), have mass M and rotational inertia I_y about the *y*-axis. The masses are connected by longitudinal massless beams directed along the *x*-axis and having flexural stiffness D. In addition, they are elastically constrained by lateral massless beams, aligned with the *y*-axis, having flexural stiffness $\hat{D}$. The influence of gravity is neglected in what follows.

(a) Governing equations

The *m-th* mass has two degrees of freedom, the transverse displacement u_m along the *z*-axis and the rotation θ_m^y about the *y*-axis (figure 1). By $U_m(x,t)$, we indicate the transverse displacement of the massless beam aligned with the *x*-direction that connects the masses positioned at $x = lm$ and $x = l(m+1)$.[1] The functions $U_m^{(+)}(y,t)$ and $U_m^{(-)}(y,t)$ are used to represent the transverse displacements in the lateral beams aligned with the *y*-axis.[2]

[1] $U_m(x,t)$ should be defined in the interval $lm + d/2 \le x \le l(m+1) - d/2$, where d is the typical size of the mass. Since $d/l \ll 1$ we neglect the dimension d in the computations.

[2] As for $U_m(x,t)$, we define $U_m^{(+)}(y,t)$ and $U_m^{(-)}(y,t)$ in the intervals $0 \le y \le L$ and $-L \le y \le 0$, respectively, neglecting the dimension d in the computations.

The dynamic behaviour of the microstructured medium is governed by the momentum balances of the *m-th* mass inside the structure. The linear momentum balance has the form

$$M\ddot{u}_m(t) = \mathcal{V}_m^x(0,t) - \mathcal{V}_{m-1}^x(l,t) + \mathcal{V}_m^{y,+}(0,t) - \mathcal{V}_m^{y,-}(L,t) + \mathcal{P}_m, \tag{2.1}$$

where the dot denotes the derivative with respect to time, $\mathcal{P}_m$ is an external transverse force and $\mathcal{V}_m^x$ and $\mathcal{V}_m^{y,\pm}$ are the shear forces transmitted by the elastic ligaments; they are shown in figure 1*b* and detailed in the electronic supplementary material. The balance of angular momentum about the *y*-axis is

$$I_y\ddot{\theta}_m^y(t) = \mathcal{M}_m^y(0,t) - \mathcal{M}_{m-1}^y(l,t) + \mathcal{M}_m, \tag{2.2}$$

where $\mathcal{M}_m$ is an external bending moment and $\mathcal{M}_m^y$ are the bending moments transmitted by the longitudinal ligaments, as shown in figure 1*b*.

We assume that the masses do not rotate about the *x*-axis as the structure vibrates. In this case, neglecting the torsional contribution of the longitudinal elements, the angular momentum balance about the *x*-axis reduces to the trivial identity

$$\mathcal{M}_m^{x,+}(0,t) = \mathcal{M}_m^{x,-}(L,t), \tag{2.3}$$

where $\mathcal{M}_m^{x,\pm}$ are the bending moments transmitted by the lateral ligaments (figure 1*b*).[3] The uncoupled problems concerning longitudinal and transverse vibrations along the *x*-axis and *y*-axis are not considered.

The above equations can be expressed in terms of the generalized coordinates governing the motions of the masses in the structure. As shown in the electronic supplementary material, (2.1) and (2.2) are written in terms of kinematic variables as follows

$$\left.\begin{aligned} &M\ddot{u}_m(t) = -\frac{6D}{l^3}\{2[2u_m(t) - u_{m+1}(t) - u_{m-1}(t)] - l[\theta_{m+1}^y(t) - \theta_{m-1}^y(t)]\} - \frac{24}{L^3}\hat{D}u_m(t) + \mathcal{P}_m \\ \text{and} \quad &I_y\ddot{\theta}_m^y(t) = -\frac{2D}{l^2}\left[3(u_{m+1}(t) - u_{m-1}(t)) + l(\theta_{m+1}^y(t) + \theta_{m-1}^y(t) + 4\theta_m^y(t))\right] + \mathcal{M}_m. \end{aligned}\right\} \tag{2.4}$$

From here on we neglect the external actions $\mathcal{P}_m$ and $\mathcal{M}_m$, $m \in \mathbb{Z}$.

3. Rayleigh beam on an elastic foundation

In the long-wavelength limit, the structure in figure 1 approximates the Rayleigh beam on an elastic foundation. As shown in the electronic supplementary material, within the low-frequency regime, the equations (2.4) governing the motion of the structure approximate the equation

$$\mu_{\text{eff}}\frac{\partial^2 u(x,t)}{\partial t^2} + D_{\text{eff}}\frac{\partial^4 u(x,t)}{\partial x^4} - \mathcal{J}_{\text{eff}}\frac{\partial^4 u(x,t)}{\partial t^2 \partial x^2} + \varkappa_{\text{eff}}u(x,t) = 0, \tag{3.1}$$

representing a Rayleigh beam resting on an elastic foundation (see, for example, [4]). Here, the effective quantities associated with a continuous beam are the density per unit length $\mu_{\text{eff}} = M/l$, the flexural stiffness $D_{\text{eff}} = D$, the rotational inertia of the cross-section $\mathcal{J}_{\text{eff}} = I_y/l$ and the stiffness of the elastic foundation $\varkappa_{\text{eff}} = 24\hat{D}/(L^3 l)$.

[3]For slender ligaments, the torsional stiffness is negligible with respect to the flexural one. The torsional contribution of the lateral ligaments implies an increase of the coefficient of θ_m^y on the right-hand side of the angular momentum balance equation in (2.4). The uncoupled torsional problem associated with rotations about the *x*-axis is not analysed here.

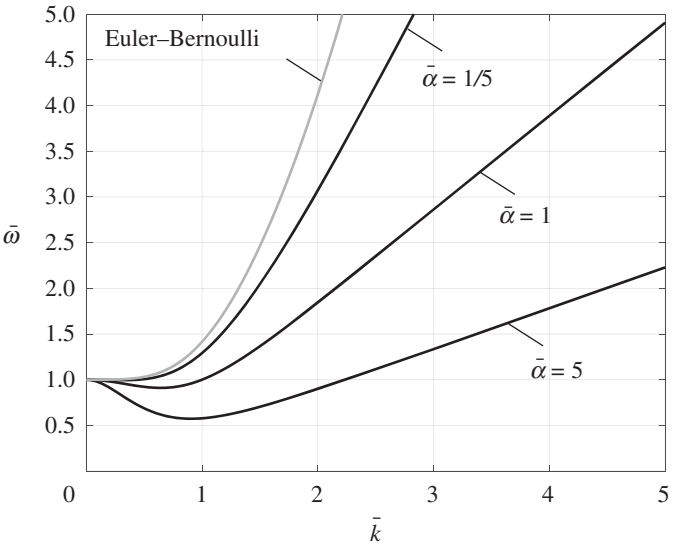

Figure 2. Dispersion curves for a Rayleigh beam on an elastic foundation based on the normalized dispersion equation (3.4). Each curve is associated with a different value of $\bar{\alpha}$ in (3.3). The grey curve ($\bar{\alpha} = 0$) corresponds to the classical elastically supported Euler–Bernoulli beam.

(a) Dispersion properties

Considering time-harmonic motions in connection with the Rayleigh beam governing equation (3.1) leads to the dispersion relation

$$\omega(k) = \sqrt{\frac{D_{\text{eff}}k^4 + \varkappa_{\text{eff}}}{\mu_{\text{eff}} + \mathcal{J}_{\text{eff}}k^2}}, \tag{3.2}$$

(see [4, Section 3.4] and [25]). Introducing

$$\bar{\omega} = \omega\sqrt{\frac{\mu_{\text{eff}}}{\varkappa_{\text{eff}}}}, \quad \bar{k} = k\left(\frac{D_{\text{eff}}}{\varkappa_{\text{eff}}}\right)^{1/4} \quad \text{and} \quad \bar{\alpha} = \sqrt{\frac{\mathcal{J}_{\text{eff}}^2\varkappa_{\text{eff}}}{\mu_{\text{eff}}^2 D_{\text{eff}}}}, \tag{3.3}$$

we obtain the normalized dispersion relation

$$\bar{\omega}(\bar{k}) = \sqrt{\frac{\bar{k}^4 + 1}{1 + \bar{\alpha}\bar{k}^2}}. \tag{3.4}$$

This function is shown in figure 2. All curves have at the cut-off frequency at the minimum located at

$$(\bar{k}^*, \bar{\omega}(\bar{k}^*)) = \sqrt{\frac{\sqrt{\bar{\alpha}^2 + 1} - 1}{\bar{\alpha}}}\left(1, \sqrt{\frac{2}{\bar{\alpha}}}\right). \tag{3.5}$$

Interestingly, the group velocity is negative in the interval $0 < \bar{k} < \bar{k}^*$ and bounded above by $\bar{\alpha}^{-1/2}$, for large $\bar{k}$. If $\bar{\alpha} = 0$, then the dispersion curve reduces to that for the classical case of an EB beam on an elastic foundation and the corresponding dispersion curve is the grey line in figure 2.

Below, we consider waves propagating in the multi-structure of §2. We will show the analogies between the continuous and discrete media considered here and the additional features introduced by the microstructure, including degeneracies where Dirac points can occur.

4. Wave propagation in the multi-structure

We return now to the elastically supported flexural multi-structure considered in §2 (figure 1). The displacements and rotations at the nodal points satisfy the governing equations (2.4). We search for nodal displacements and rotations in the form

$$u_m(t) = U e^{i(\omega t - klm)} \quad \text{and} \quad \theta_m^y = \Theta^y e^{i(\omega t - klm)},$$

where ω is the frequency of vibration and k the wavenumber. The following normalization is adopted:

$$\tilde{\omega} = \sqrt{\frac{Ml^3}{D}}\omega, \quad \tilde{u}_m = \frac{u_m}{l}, \quad \tilde{I} = \frac{I_y}{Ml^2} \quad \text{and} \quad \tilde{k} = kl.$$

In going forward, the tilde will be omitted for ease of notation unless otherwise stated. Then, in the absence of external loads, balances (2.4) lead to

$$-\omega^2 U = -6\{4[1-\cos(k)]U + 2i\sin(k)\Theta^y\} - 24rU \tag{4.1}$$

and

$$-I\omega^2\Theta^y = -2\left[-6i\sin(k)U + 2\Theta^y(2+\cos(k))\right], \tag{4.2}$$

with the following definition of the normalized stiffness of the supports:

$$r = \frac{l^3}{L^3}\frac{\hat{D}}{D}.$$

We then have

$$\Theta^y = \frac{12i\sin(k)U}{I\mathcal{F}(k, i\omega)}, \quad \text{where } \mathcal{F}(k,s) = (\omega_0(k))^2 + s^2, \quad \omega_0(k) = \sqrt{\frac{4(2+\cos(k))}{I}} \tag{4.3}$$

that is combined with (4.1) to obtain

$$\zeta(k, i\omega)U = 0, \tag{4.4}$$

where

$$\zeta(k,s) = s^4 + 2a(k)s^2 + b(k),$$
$$a(k) = \frac{2}{I}\left[2+\cos(k) + 6I\left\{r + 2\sin^2\left(\frac{k}{2}\right)\right\}\right], \quad b(k) = \frac{96}{I}\left[2\sin^4\left(\frac{k}{2}\right) + r(2+\cos(k))\right]. \tag{4.5}$$

(a) Dispersion properties of a supported mass-beam chain

Free waves inside the structure are determined from the non-trivial solutions of the homogeneous equation (4.4). Such solutions correspond to zeros of the function ζ in (4.4), which is satisfied when the radian frequency is

$$\omega^{(\pm)} = \left[a(k) \pm \sqrt{(a(k))^2 - b(k)}\right]^{1/2}. \tag{4.6}$$

Note that the expression under the radical of $(\omega^{(\pm)})^2$ is non-negative for any real k. We also have the inequality

$$0 < \omega^{(-)}(k) \le \omega_0(k) \le \omega^{(+)}(k), \tag{4.7}$$

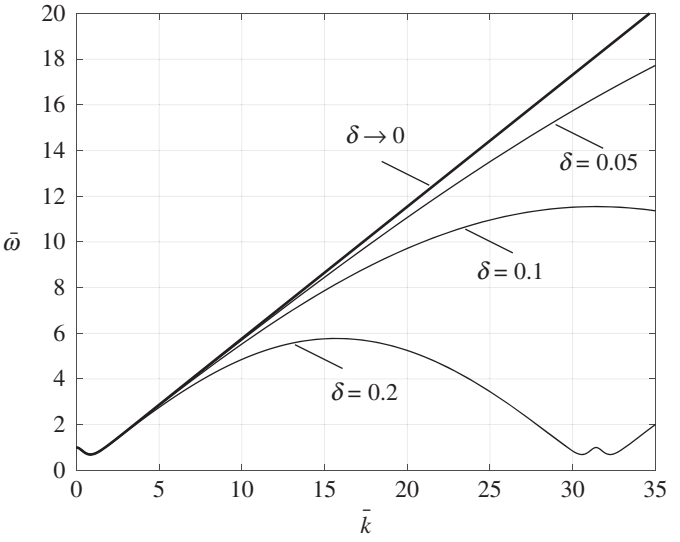

Figure 3. Dispersion curves $\omega^{(-)}$ (see (4.6)) for the multi-structure ($\delta > 0$) and the effective Rayleigh beam ($\delta \to 0$). Results are given for $\bar{\alpha} = 3$ and $\delta = 0.05, 0.1, 0.2$ (see (4.8) and (4.9)).

where $\omega_0(k)$ is defined in (4.3). A comparison between $\omega^{(-)}$ defined in equation (4.6) and the dispersion curve for the Rayleigh beam based on (3.4) is reported in figure 3. In the comparison, we used the conversions

$$k = \bar{k}\delta, \quad \bar{\omega} = \frac{\omega^{(-)}}{\delta^2}, \; r = \frac{1}{24}\delta^4 \quad \text{and} \quad I = \frac{\bar{\alpha}}{\delta^2},$$

where the dimensionless frequency $\bar{\omega}$ and wavenumber $\bar{k}$ for the Rayleigh beam and $\bar{\alpha}$ were introduced in equation (3.3). The dimensionless parameter

$$\delta = l\left(\frac{\varkappa_{\text{eff}}}{D_{\text{eff}}}\right)^{1/4} \tag{4.8}$$

is the ratio between the length scale in the multi-structure to the typical length scale of the continuum approximation. Moreover, we have also assumed the following choices for the micro-structural parameters

$$\hat{D} = \hat{D}_0\delta, \quad I_y = I_0\delta \quad \text{and} \quad M = M_0\delta.$$

Therefore, according to § 3, we have

$$\varkappa_{\text{eff}} = \left(\frac{24\hat{D}_0}{L^3 D^{1/4}}\right)^{4/3} \quad \text{and} \quad \bar{\alpha} = \frac{I_0}{M_0 L^2}\left(\frac{24\hat{D}_0}{D}\right)^{2/3}. \tag{4.9}$$

We note in figure 3, in taking $\delta \to 0$ (the long-wavelength regime), $\omega^{(-)}$ converges to the dispersion curve for the continuous Rayleigh beam (3.4), as expected on physical grounds. On the other hand, $\omega^{(+)}$ diverges.

Polarization of the eigenmodes is briefly discussed in part (c) of the electronic supplementary material.

(i) Parametric study of dispersion properties

Here, the influence of the normalized moment of inertia I and the normalized stiffness of the supports r on the dispersive properties of the discrete medium is discussed in detail. The structure admits two dispersion curves, in contrast with the microstructured EB type model [18],

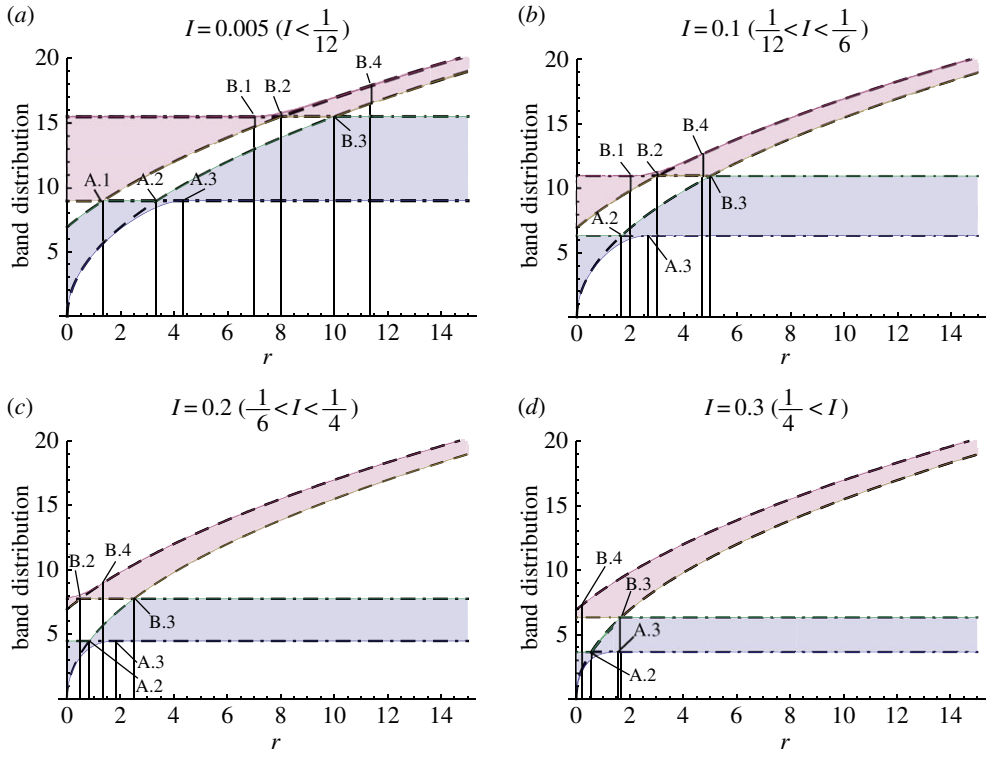

Figure 4. Band distributions as a function of the stiffness r of the supporting beams in the multi-structure for (*a*) $I = 0.05$, (*b*) $I = 0.1$, (*c*) $I = 0.2$ and (*d*) $I = 0.3$. The blue and pink regions correspond to the acoustic and optical passbands, respectively. Dashed lines indicate the bounds of the band of the corresponding elastically supported EB structure ($I = 0, r \neq 0$), dot-dashed lines indicate the bounds of the band for an unsupported structure with rotational inertia ($r = 0, I \neq 0$). The points A.1 to A.3 and B.1 to B.4 are defined in table 1. (Online version in colour.)

corresponding to the limit $I \to 0$, and to the continuous EB and Rayleigh beam models, where only a single dispersion curve exists. The extra band reflects the presence of the rotational inertia I at the junctions, leading to the system being capable of supporting additional vibrations and failure modes (see [15]). The second band reflects the interaction of the waves with the internal microstructure at the meso-scale. Namely, it can be identified with Bragg scattering. As shown in the previous section, the second band is absent in the continuum limit, since $\omega^{(+)}$ diverges when $k \to 0$.

For the band distribution of the structure, we distinguish three different classes of regimes in the parametric space defined by I and r. These regimes are

— low stiffness r in the supports (LS) and/or low rotational inertia I of the masses (LI);
— high stiffness (HS) and/or high rotational inertia (HI);
— a transition one.

In figure 4, we show the band distribution as a function of r, for different values of I, while in figure 5 the band distribution is shown as a function of I for different values of r. The values of the critical points A.1 to A.3 and B.1 to B.4 in the (r, I) parametric space are reported in table 1.

In the lower (LI, LS) and higher (HS, HI) regimes, the two passbands depend on a single parameter, either r or I. One band matches the band of an elastically supported EB structure without rotational inertia, whose bounds are indicated with dashed lines in figures 4 and 5, whereas the other matches the band of the unsupported structure with rotational inertia, whose

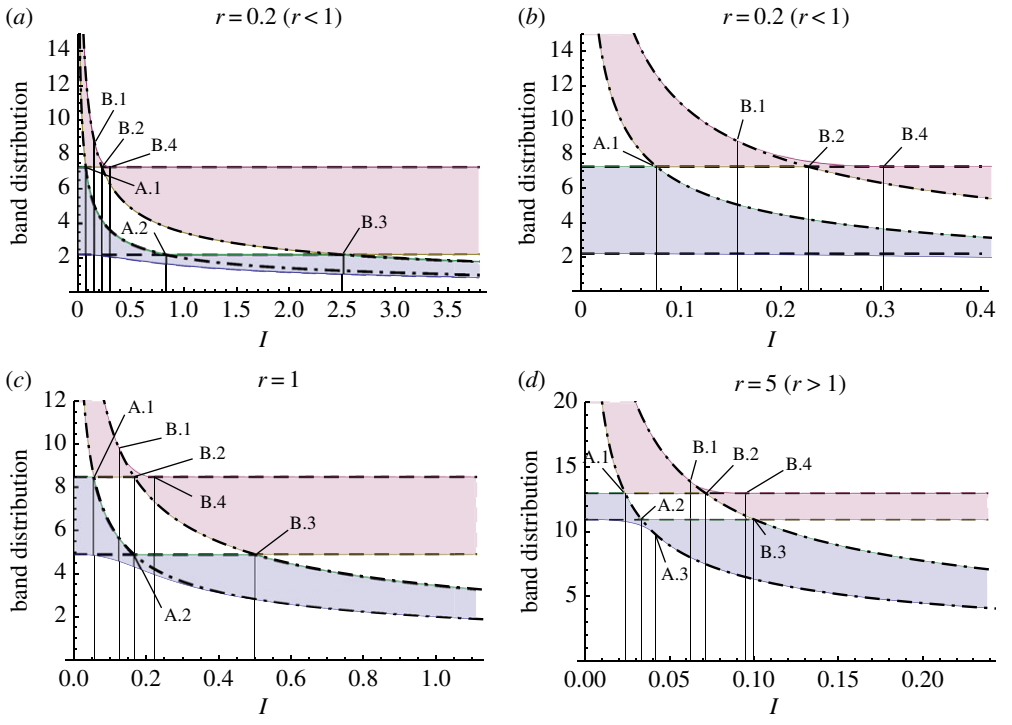

Figure 5. Band distributions as a function of the moment of inertia I of the nodal points in the multi-structure for (*a*), (*b*) $r = 0.2$ ((*b*) contains a magnification of (*a*)), (*c*) $r = 1$ and (*d*) $r = 5$. The blue and pink regions correspond to the acoustical and optical passbands, respectively. Dashed lines indicate the bounds of the band of the corresponding elastically supported EB structure ($I = 0, r \neq 0$), dot-dashed lines indicate the bounds of the band for an unsupported structure with rotational inertia ($r = 0, I \neq 0$). The points A.1 to A.3 and B.1 to B.4 indicated in each figure are given in table 1. (Online version in colour.)

Table 1. Critical points in the band diagrams in figures 4 and 5 in terms of I and r.

point	A.1	A.2	A.3	B.1	B.2	B.3	B.4
r	$\frac{1}{6I} - 2$	$\frac{1}{6I}$	$\frac{1}{6I} + 1$	$\frac{1}{2I} - 3$	$\frac{1}{2I} - 2$	$\frac{1}{2I}$	$\frac{2}{3I} - 2$
I	$\frac{1}{6(r+2)}$	$\frac{1}{6r}$	$\frac{1}{6(r-1)}$	$\frac{1}{2(r+3)}$	$\frac{1}{2(r+2)}$	$\frac{1}{2r}$	$\frac{2}{3(r+2)}$

bounds are indicated with dot-dashed lines. In the LI and LS regimes, the acoustical band is governed by r and the optical band by I. On the other hand, in the HI and HS regimes, the dependency is the contrary and the high rotational inertia induces a low-frequency acoustic band of finite width. Such a configuration suggests possible applications to the construction of metamaterials with arrays of resonators, which are usually limited in their technological application as they possess narrow bands [1,26–29].

Clearly, for $r > 0$, there is a zero frequency stop band with the cut-off frequency $\min \omega^{(-)}(k)$. In the next subsection, we will detail the position of this minimum in the reciprocal space. The LI and LS regimes exist for $r > 0, I > 0$ and are bounded above by the point A.1 (table 1), provided $I < 1/12$ (figure 4*a*), otherwise these regimes are not present (figures 4*b–d*). The HS and HI regimes are bounded below by the maximum of the points B.3 and A.3 with respect to I and r. Different cases are shown in figures 4 and 5 based on the data in table 1. The maximum is B.3 if $I < 1/3$ and A.3 otherwise and B.3 if $r > 3/2$ and A.3 otherwise. Note that, depending on the values of the non-negative parameters r and I, the lower and upper band can strictly coincide with the EB ($I = 0$) or unsupported ($r = 0$) cases. In the two intervals bounded by the points B.1 and B.4 and

above by the point A.3 there are small differences; such cases are associated with the emergence of an additional stationary point within the first Brillouin zone.

The intermediate regime, located between A.1 and the maximum between A.3 and B.3, admits the scenario where the two bands interact to reduce the width of or remove the central stop band. In this regime, the pass bands can also merge to form a single pass band in correspondence of the Dirac points A.1 and B.3 (see [30–33]).

Within this regime, the finite width of the central band gap is modulated by r and I. The maximum width is achieved when $r \geq 1$ and $I \geq 1/6$. It is equal to the width of the EB passband for $r \geq 1$ (figure 5*c*,*d*), and to the width of the unsupported structure for $I \geq 1/6$ (figure 4*c*,*d*). It is noted that B.2 is not defined if $I \geq 1/4$.

In order to maximize the filtering properties of the system, we can minimize the width of the passbands, as shown in the vicinity of A.2 and B.2 in figures 4 and 5. The filtering properties of the structure are maximized when these points coincide for $(r, I) = (1, 1/6)$. In this case, the total width of the frequency intervals supporting waves inside the structure reaches a minimum, limiting possibilities for wave propagation into the medium.

We consider now the case where the masses of the nodes are small with respect to the inertia I_y. This configuration is difficult to obtain: for example, in the case of cubic nodes with dimension d, $(Ml^2)/I_y \simeq 10 * (l/d)^2 \gg 1$. Then, with the adoption of a different normalization, it can be shown that, when $(Ml^2)/I_y \to 0$, the band corresponding to elastically supported EB structures diverges to infinity and a single dispersion curve remains. This result is consistent with the behaviour, when $k \to 0$, of the dispersion relation (3.2) for the long-wavelength limit.

In classical EB structures, two passbands can be obtained by introducing two types of masses, but in such a case, the interaction between the passbands in the transition regime is not present. The transition regime obtained here incorporates finite stop bands governed by the limiting cases $I \to 0$ and $r = 0$ and the appearance of Dirac points. Moreover, the proposed microstructure may exhibit additional stationary points along the dispersion curves inside the first Brillouin zone and not only at the boundaries of the zone. The presence of these additional stationary points may lead to the initiation and support of several distinct classes of failure regimes in the medium [15].

(ii) Special properties of the dispersion curves

Stationary points of dispersion curves. The solutions $\omega^{(\pm)}$ in equation (4.6) can have stationary points in the interior of the Brillouin zone. We define the wavenumbers $k_\pm$ by

$$k_\pm = 2 \arctan \left[\frac{X - 8(6I+1)(3I(r+1)-1) \pm 6|6I-1|\sqrt{Y}}{X \mp 6|6I-1|\sqrt{Y}} \right]^{1/2}, \tag{4.10}$$

where

$$X = 2[6Ir(6I+1) + 6I(12I-5) - 1] \quad \text{and} \quad Y = 12I^2 r(r+2) - 8Ir + 1.$$

Domains in the (r, I) space, where the stationary points exist, are indicated by I–IV in figure 6.

For $I > 0$, $0 < r < (1+6I)/(6I)$ the function $\omega^{(-)}$ has a global minimum at the wavenumber

$$k = \begin{cases} k_- & \text{if } I \leq \frac{1}{6}, \\ k_+ & \text{if } I > \frac{1}{6}, \end{cases} \tag{4.11}$$

that is located inside the irreducible Brillouin zone. With regard to figures 4 and 5, this global minimum occurs in the interval defined between the point $(r, I) = (0, 0)$ and the point A.3. Note that in figure 5 this point exists if $r > 1$.

The global maximum for the function $\omega^{(+)}$ is in the interior of the Brillouin zone if $I \leq 1/3$ and $(1-6I)/(2I) < r < 2(1-3I)/(3I)$. These stationary points appear between the points B.1 and B.4 indicated in figures 4 and 5. The wavenumber corresponding to this point is

$$k = \begin{cases} k_+ & \text{if } I \leq \frac{1}{6} \\ k_- & \text{if } I > \frac{1}{6} \end{cases}. \tag{4.12}$$

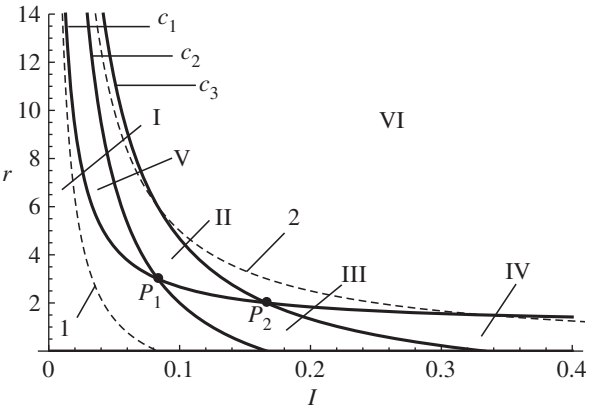

Figure 6. Domains I–VI in the (r, I) space where the dispersion curves $\omega^{(\pm)}$ have stationary points of a different nature. In domains {I, III, IV} and {II, III}, $\omega^{(-)}$ and $\omega^{(+)}$ exhibits a global minimum and maximum in the interior of the first Brillouin zone, respectively. Solid curves c_1, c_2 and c_3 represent the boundaries of these regions indicated by I–VI. The dashed curves 1 and 2 indicate the emergence of Dirac points. Regions V and VI correspond to the typical cases when $\omega^{(\pm)}$ reaches the extremal values at the boundaries of the first Brillouin zone. Typical dispersion curves corresponding to each region are reported in figure 7.

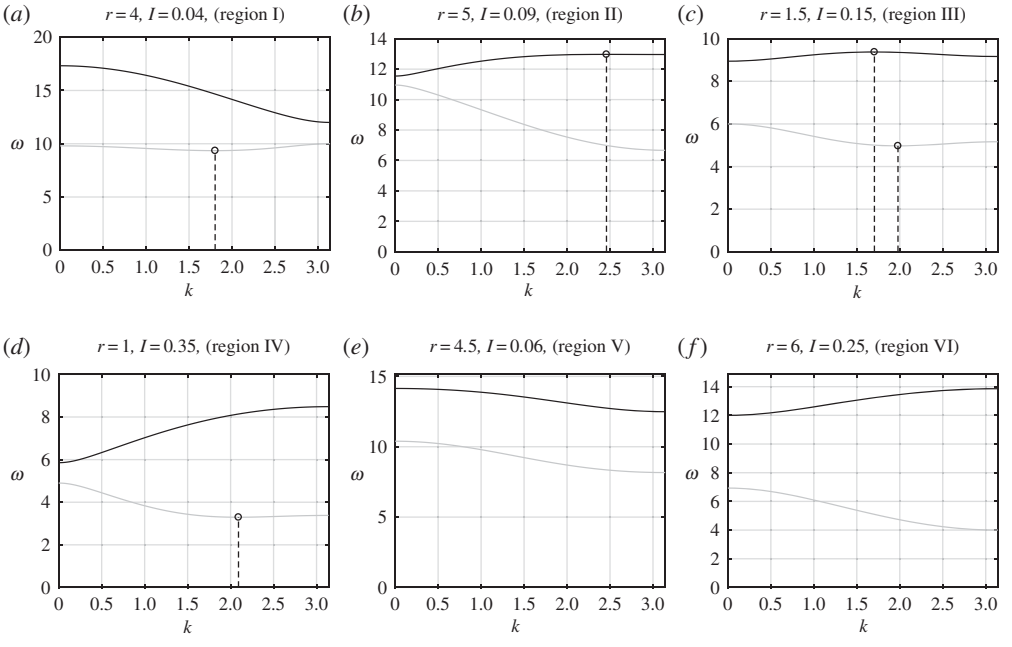

Figure 7. Dispersion curves in the first Brillouin zone. Each diagram is a representative of the dispersion curves in regions (specified in figure 6) I to VI in (*a*) to (*f*), respectively. The wavenumbers $k_\pm$, given in (4.11), (4.12) are also shown and correspond to the stationary points indicated by circles.

In regions I, II and IV, there is only one interior stationary point belonging to either $\omega^{(-)}$ or $\omega^{(+)}$. In regions I and IV, the coordinates of the global minimum are $(k_-, \omega^{(-)}(k_-))$ and $(k_+, \omega^{(-)}(k_+))$, respectively, whereas in region II the global maximum is at $(k_+, \omega^{(+)}(k_+))$. Examples corresponding to these cases are shown in figures 7*a*,*d* and *b*, respectively.

In region III, starting at $P_1 = (1/12, 3)$ in figure 6, both global maximum and minimum are in the interior of the first Brillouin zone, as reported in figure 7*c*. Inside this region, for $1/12 < I \leq 1/6$ the coordinates of the stationary points are $(k_-, \omega^{(-)}(k_-))$ and $(k_+, \omega^{(+)}(k_+))$, while for $I > 1/6$ the

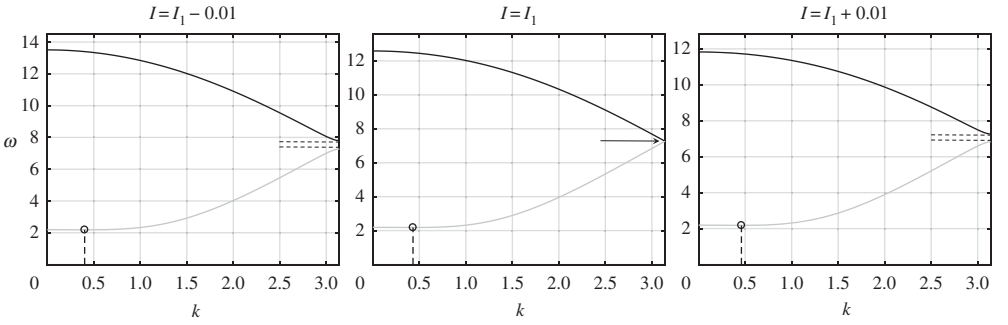

Figure 8. Dispersion curves based on (4.6) showing the effect of perturbation of the rotational inertia from $I = I_1$ in equation (4.13). Computations are performed for $r = 1/5$.

coordinates of these points are $(k_+, \omega^{(-)}(k_+))$ and $(k_-, \omega^{(+)}(k_-))$ and the wavenumbers $k_\pm$ have been interchanged. Moreover, if $1/12 < I \leq 1/6$, and r is increased inside region III, the stationary points $k_\pm$ for $\omega^{(\pm)}$ move from 0 to π inside the Brillouin zone. In particular, $I = 1/6$ represents a critical value where this interchange of k_+ and k_- occurs and the wavenumbers of the stationary points coincide.

The regions V and VI in figure 6 correspond to the case where $k_\pm$ in (4.11) and (4.12) are not real and the dispersion curves retain the classical stationary points at the boundary of the Brillouin zones (figures 7*e*,*f*). Curves c_1, c_2 and c_3 are associated with the points A.3, B.1 and B.4 in table 1. The point $P_1 = (1/12, 3)$ is the intersection between c_1 and c_2 and the point $P_2 = (1/6, 2)$ is the intersection between c_1 and c_3. In moving from either $I = 0$ or $r = 0$ to the curve c_1 the global minimum in $\omega^{(-)}$ shifts from $k = 0$ to $k = \pi$. In moving from c_2 to c_3 the global maximum of $\omega^{(+)}$ moves from $k = 0$ to $k = \pi$. In particular, above the curve c_1 in the (r, I) space, $\omega^{(-)}$ has a global minimum at $k = \pi$ and a global maximum at $k = 0$. Below c_2 (above c_3), $\omega^{(+)}$ has a global maximum (minimum) at $k = 0$ and global minimum (maximum) at $k = \pi$.

In addition, the curves 1 and 2 shown in figure 6 define r and I values where Dirac points occur at the boundary of the irreducible Brillouin zone.

(iii) Degeneracies at the edges of the Brillouin zone: Dirac points

Within the transition regime one can open a stop band, whose width can be controlled by adjusting the stiffness of the supports and the moment of inertia of the masses. At the points A.1 and B.3 of figures 4 and 5, the stop band can be closed. The points are associated with the values

$$I_1 = \frac{1}{6(r+2)} \quad \text{and} \quad I_2 = \frac{1}{2r}. \tag{4.13}$$

When the stop band closes at A.1 and B.3, Dirac points emerge at $k = 0$ and $k = \pi$ in the dispersion curves, respectively. At these points, the group velocity associated with the dispersion curves is discontinuous, as shown in figures 8 and 9. The Dirac points arise when I and r are chosen to be situated along curves 1 and 2 in figure 6.

Figure 8 demonstrates how the Dirac point emerges at $k = \pi$ for a particular value of r, when I is chosen in the vicinity of I_1. There, it is clear that when $I = I_1$ the Dirac point is situated at π (indicated by an arrow in the central panel of figure 8). The value of frequency at which the Dirac point occurs is

$$\omega = 2\sqrt{6(r+2)}, \tag{4.14}$$

and the group velocity of $\omega^{(-)}$ ($\omega^{(+)}$) as $k = \pi$ is approached from the left and the right is ± 3 (∓ 3). Thus, the frequency (4.14) is dependent on the material parameters of the structure, whereas the group velocity from the left and the right of the Dirac point is not.

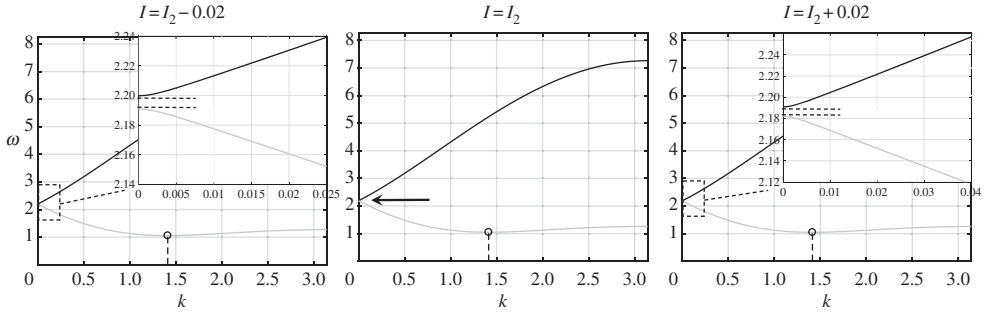

Figure 9. Dispersion curves based on (4.6) showing the effect of perturbation of the rotational inertia from $I = I_2$. Computations are performed for $r = 1/5$.

Similar features can be observed for $I = I_2$ where the Dirac point is located at $k = 0$, (see central panel of figure 9). The value of frequency where this Dirac point appears is

$$\omega = 2\sqrt{6r},$$

which is smaller than the frequency (4.14). Additionally, the group velocity of $\omega^{(-)}$ ($\omega^{(+)}$) as $k \to 0$ from the left and right is $\pm\sqrt{3}$ ($\mp\sqrt{3}$), and these values are again independent of r.

Perturbing I about value I_2 leads to a stop band emerging at $k = 0$; the effect is not as strong as in the case when I is close to I_1.

5. Conclusion

We have determined the dispersion properties of a discretely supported flexural system possessing rotational inertia, representing a simplified model of a civil engineering structure such as a bridge [14].

In the long-wavelength regime, this medium can be interpreted as a continuous Rayleigh beam, with a continuous distribution of rotational inertia, resting on a Winkler foundation. The rotational inertia of the microstructure provides the medium with the potential to support high-frequency waves, that can trigger and support additional failure modes of the medium (see [15]). The presence of additional stationary points in the irreducible Brillouin zone has been fully described, since it can influence the dynamic propagation of failure.

Three different regimes have been identified in the parametric space (I, r), where the acoustic and the optical modes may interact to a different extent. By modulating the rotational inertia I and the support stiffness r, it is possible to maximize the filtering properties of the mechanical system opening large band gaps at low frequencies, a property that confirms the findings in [1].

The complete study of the interplay between the parameters governing the stiffness of the supports and the rotational inertia has revealed a variety of important dynamic properties possessed by the structure, which also includes dispersion degeneracies currently driving the design of efficient topological insulators for earthquake protection [34,35]. This investigation has provided a recipe for manipulating the properties of the medium to obtain dynamic properties for a variety of technological applications.

Interestingly, while the frequency at Dirac points is governed by the rotational inertia and support stiffness the group velocity at these points is not.

Data accessibility. This article has no additional data.

Authors' contributions. M.J.N. performed the analytical and numerical computations for the work. M.B. performed part of the numerical computations. All the authors contributed to the development of the model and the preparation of the manuscript.

Competing interests. We declare we have no competing interests.

Funding. M.J.N and M.B. gratefully acknowledge the support of the EU H2020 grant no. MSCA-IF-2016-747334-CAT-FFLAP.

References

1. Carta G, Brun M. 2015 Bloch–Floquet waves in flexural systems with continuous and discrete elements. *Mech. Mater.* **87**, 11–26. (doi:10.1016/j.mechmat.2015.03.004)
2. Gei M, Movchan AB, Bigoni D. 2009 Band-gap shift and defect-induced annihilation in prestressed elastic structures. *J. Appl. Phys.* **105**, 063507. (doi:10.1063/1.3093694)
3. Carta G, Brun M, Movchan AB. 2014 Dynamic response and localisation in strongly damaged waveguides. *Proc. R. Soc. A* **470**, 20140136. (doi:10.1098/rspa.2014.0136)
4. Graff KF. 1975 *Wave motion in elastic solids*. New York, NY: Dover Publications.
5. Piccolroaz A, Movchan AB, Cabras L. 2017 Rotational inertia interface in a dynamic lattice of flexural beams. *Int. J. Solids Struct.* **112**, 43–53. (doi:10.1016/j.ijsolstr.2017.02.023)
6. Piccolroaz A, Movchan AB, Cabras L. 2017 Dispersion degeneracies and standing modes in flexural waves supported by Rayleigh beam structures. *Int. J. Solids Struct.* **109**, 152–165. (doi:10.1016/j.ijsolstr.2017.01.017)
7. Cabras L, Movchan AB, Piccolroaz A. 2017 Floquet-Bloch waves in periodic networks of the Rayleigh beams: honeycomb systems, dispersion degeneracies and structured interfaces. *Mech. Sol., A J. Russ. Acad. Sci.* **5**, 93–108. (doi:10.3103/s0025654417050107)
8. Bordiga G, Cabras L, Piccolroaz A, Bigoni D. 2019 Prestress tuning of negative refraction and wave channeling from flexural sources. *Appl. Phys. Lett.* **114**, 041901. (doi:10.1063/1.5084258)
9. Bordiga G, Cabras L, Bigoni D, Piccolroaz A. 2019 Free and forced wave propagation in a Rayleigh-beam grid: flat bands, Dirac cones, and vibration localization vs isotropization. *Int. J. Solids Struct.* **161**, 64–81. (doi:10.1016/j.ijsolstr.2018.11.007)
10. Bacigalupo A, Gambarotta L. 2016 Simplified modelling of chiral lattice materials with local resonators. *Int. J. Solids Struct.* **83**, 126–141. (doi:10.1016/j.ijsolstr.2016.01.005)
11. Bacigalupo A, Gambarotta L. 2017 Wave propagation in non-centrosymmetric beam-lattices with lumped masses: discrete and micropolar modeling. *Int. J. Solids Struct.* **118–119**, 128–145. (doi:10.1016/j.ijsolstr.2017.04.010)
12. Bacigalupo A, Lepidi M. 2016 High-frequency parametric approximation of the Floquet–Bloch spectrum for anti-tetrachiral materials. *Int. J. Solids Struct.* **97–98**, 575–592. (doi:10.1016/j.ijsolstr.2016.06.018)
13. Brun M, Giaccu GF, Movchan AB, Movchan NV. 2012 Asymptotics of eigenfrequencies in the dynamic response of elongated multi-structures. *Proc. R. Soc. Lond. A* **468**, 378–394. (doi:10.1098/rspa.2011.0415)
14. Carta G, Giaccu GF, Brun M. 2017 A phononic band gap model for long bridges. The 'Brabau' bridge case. *Eng. Struct.* **140**, 66–76. (doi:10.1016/j.engstruct.2017.01.064)
15. Slepyan LI. 2002 *Models and phenomena in fracture mechanics*. Berlin, Germany: Springer.
16. Ryvkin M, Slepyan LI. 2010 Crack in a 2D beam lattice: analytical solutions for two bending modes. *J. Mech. Phys. Solids* **58**, 902–917. (doi:10.1016/j.jmps.2010.03.006)
17. Ryvkin M. 2012 Analytical solution for a mode III crack in a 3D beam lattice. *Int. J. Solids Struct.* **49**, 2839–2847. (doi:10.1016/j.ijsolstr.2012.04.003)
18. Brun M, Movchan AB, Slepyan LI. 2013 Transition wave in a supported heavy beam. *J. Mech. Phys. Solids* **61**, 2067–2085. (doi:10.1016/j.jmps.2013.05.004)
19. Movchan AB, Brun M, Slepyan LI, Giaccu GF. 2015 Dynamic multi-structure in modelling a transition flexural wave. *Mathematika* **61**, 444–456. (doi:10.1112/S0025579314000321)
20. Brun M, Giaccu GF, Movchan AB, Slepyan LI. 2014 Transition wave in the collapse of the San Saba bridge. *Front. Mater.* **1**, 12. (doi:10.3389/fmats.2014.00012)
21. Nieves MJ, Mishuris GS, Slepyan LI. 2016 Transient wave in a transformable periodic flexural structure. *Int. J. Solids Struct.* **112**, 185–208. (doi:10.1016/j.ijsolstr.2016.11.012)
22. Nieves MJ, Mishuris GS, Slepyan LI. 2016 Analysis of dynamic damage propagation in discrete beam structures. *Int. J. Solids Struct.* **97–98**, 699–713. (doi:10.1016/j.ijsolstr.2016.02.033)
23. Cherkaev A, Ryvkin M. 2019 Damage propagation in 2d beam lattices: 1. Uncertainty and assumptions. *Arch. Appl. Mech.* **89**, 485–501. (doi:10.1007/s00419-018-1429-z)
24. Cherkaev A, Ryvkin M. 2019 Damage propagation in 2d beam lattices: 2. Design of an isotropic fault-tolerant lattice. *Arch. Appl. Mech.* **89**, 503–519. (doi:10.1007/s00419-018-1428-0)

25. Piccolroaz A, Movchan AB. 2014 Dispersion and localisation in structured Rayleigh beams. *Int. J. Solids Struct.* **25–26**, 4452–4461. (doi:10.1016/j.ijsolstr.2014.09.016)
26. Xiao Y, Wen J, Wen X. 2012 Flexural wave band gaps in locally resonant thin plates with periodically attached spring-mass resonators. *J. Phys. D: Appl. Phys.* **45**, 195401. (doi:10.1088/0022-3727/45/19/195401)
27. Xiao Y, Wen J, Yu D, Wen X. 2013 Flexural wave propagation in beams with periodically attached vibration absorbers: band-gap behavior and band formation mechanisms. *J. Sound Vib.* **332**, 867–893. (doi:10.1016/j.jsv.2012.09.035)
28. Bigoni D, Guenneau S, Movchan AB, Brun M. 2013 Elastic metamaterials with inertial locally resonant structures: application to lensing and localization. *Phys. Rev. B* **87**, 174303. (doi:10.1103/PhysRevB.87.174303)
29. Haslinger SG, Movchan NV, Jones IS, Craster RV. 2017 Controlling flexural waves in semi-infinite platonic crystals with resonator-type scatterers. *Q. J. Mech. Appl. Math.* **70**, 216–247. (doi:10.1093/qjmam/hbx005)
30. Castro-Neto AH, Guinea F, Peres NMR, Novoselov KS, Geim AK. 2009 The electronic properties of graphene. *Rev. Mod. Phys.* **81**, 109–162. (doi:10.1103/RevModPhys.81.109)
31. Pyrialakos G, Nye NS, Kantartzis NV, Christodoulides D. 2017 Emergence of type-II dirac points in graphyne like photonic lattices. *Phys. Rev. Lett.* **119**, 113901. (doi:10.1103/PhysRevLett.119.113901)
32. Chen H, Nassar H, Huang GL. 2018 A study of topological effects in 1D and 2D mechanical lattices. *J. Mech. Phys. Solids* **117**, 22–36. (doi:10.1016/j.jmps.2018.04.013)
33. McPhedran RC, Movchan AB, Movchan NV, Brun M, Smith MJA. 2015 Parabolic trapped modes and steered Dirac cones in platonic crystals. *Proc. R. Soc. A* **471**, 20140746. (doi:10.1098/rspa.2014.0746)
34. Carta G, Jones IS, Movchan NV, Movchan AB, Nieves MJ. 2017 'Deflecting elastic prism' and unidirectional localisation for waves in chiral elastic systems. *Sci. Rep.* **7**, 26. (doi:10.1038/s41598-017-00054-6)
35. Garau M, Carta G, Nieves MJ, Jones IS, Movchan NV, Movchan AB. 2018 Interfacial waveforms in chiral lattices with gyroscopic spinners. *Proc. R. Soc. Lond. A* **474**, 20180132. (doi:10.1098/rspa.2018.0132)